Parametric uncertainty in nanoscale optical dimensional measurements

James Potzick and Egon Marx*

National Institute of Standards and Technology, Gaithersburg, Maryland 20899, USA

*Corresponding author: egon.marx@nist.gov

Received 13 September 2011; revised 22 March 2012; accepted 30 March 2012; posted 2 April 2012 (Doc. ID 154474); published 4 June 2012

Image modeling establishes the relation between an object and its image when an optical microscope is used to measure the dimensions of an object of size comparable to the illumination wavelength. It accounts for the influence of all of the parameters that can affect the image and relates the apparent feature width (FW) in the image to the true FW of the object. The values of these parameters, however, have uncertainties, and these uncertainties propagate through the model and lead to parametric uncertainty in the FW measurement, a key component of the combined measurement uncertainty. The combined uncertainty is required in order to decide if the result is adequate for its intended purpose and to ascertain if it is consistent with other results. The parametric uncertainty for optical photomask measurements derived using an edge intensity threshold approach has been described previously; this paper describes an image library approach to this issue and shows results for optical photomask metrology over a FW range of 10 nm to 8 μm using light of wavelength 365 nm. The principles will be described; a one-dimensional image library will be used; the method of comparing images, along with a simple interpolation method, will be explained; and results will be presented. This method is easily extended to any kind of imaging microscope and to more dimensions in parameter space. It is more general than the edge threshold method and leads to markedly different uncertainties for features smaller than the wavelength.

OCIS codes: 120.0120, 120.3940, 180.0180, 180.5810, 110.0180, 290.3700.

1. Introduction

The work described here supports the calibration of integrated circuit photomask feature width (FW) standards at the National Institute of Standards and Technology (NIST) [1]. In this context, a photomask feature is a chrome line or space on the mask. These standards are traceable to the definition of the meter and are used to ensure the accuracy of photomask measurements in the production of electronic products around the world, improving their performance and reducing their cost [2]. Potentially, an atomic force microscope (AFM) is a good choice for this purpose because its imaging model is simpler than those for optical and electron microscopes and does not depend on material properties, but the AFM measurement process is far too labor intensive for the batch calibration of photomask standards. In practice, a transmission mode optical microscope is used for photomask FW calibrations at NIST because it is accurate, clean, automated, and relatively fast, and it does not suffer from AFM tip wear issues. Samples of the optical measurements on a control photomask are checked against AFM measurements to create a control chart and monitor system performance.

With a microscope, we can only directly measure the image of an object, not the object itself. An image is not a measurement, and we must infer the object size from the scaled image. For relatively large objects, the imaging process is nearly linear, in the sense that

$$\text{object size} = \text{scale factor} \times \text{image size} + \text{offset}.$$

Then two-point calibration can determine the *scale factor* and *offset* for subsequent measurements. When the object size becomes comparable to the

illumination wavelength used in an optical microscope, however, the imaging process becomes nonlinear with object size, resulting in measurement error when the linear model is used. Figure 1 shows simulated grayscale microscope images of isolated chrome-on-quartz photomask lines and spaces viewed in transmission at a 365 nm wavelength. The measured image intensity, normalized to 1 through clear quartz, is superimposed on each image. Figure 2, based on modeling the optical imaging process, shows the error incurred measuring the width of such features at this wavelength if two-point calibration is used; i.e., assuming that the image intensity at the chrome line edges is constant. Note the logarithmic feature width scale, which will be used throughout this paper. The imaging wavelength is indicated by the vertical dot-dash line.

Consequently, a more general procedure must be used to measure small objects optically; that is, compare the image of the object with the image of a reference object of similar and known dimensions. This reference object may be (1) a standard object whose dimensions have been measured by some other means, such as an AFM, with its own limitations and uncertainties (2) or the simulated image of an ideal object.

Since the perfect standard object does not exist, this paper will concentrate on simulated images of ideal objects that closely resemble real objects. A better way to extract data from an image would be inverse image modeling, which calculates object topography directly from the image. While relatively straightforward for AFMs, this approach is virtually impossible for optical microscopes and scanning electron microscopes (SEMs) because of the complexity of the imaging process and possible uniqueness problems.

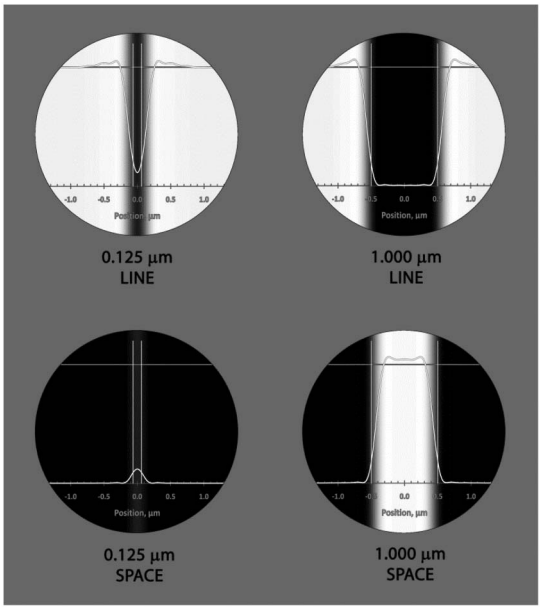

Fig. 1. Simulated microscope grayscale images of isolated 0.125 μm and 1.000 μm lines and 0.125 μm and 1.000 μm spaces viewed in transmission. Image intensity is overlaid as a graph.

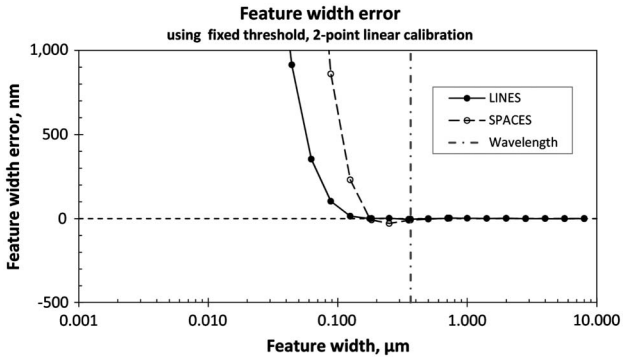

Fig. 2. FW error as function of FW. Traditional two-point (linear) calibration works well for measuring isolated features larger than the wavelength, but generates large errors for smaller objects. Note the logarithmic FW scale used throughout this paper.

We have sought to determine the combined parametric standard uncertainty using an image library. After a brief discussion on optical image modeling, the specific motivation for this work will be described, followed by a description of the variable threshold method of extracting FW information from a microscope image and its parametric uncertainty limitations, and then a description of the image library method and its benefits. A few remarks on model accuracy and completeness conclude the paper.

2. Image Modeling

Figure 2 exemplifies the benefit of image modeling. Since we wished to measure the object, but could only directly measure its image in a microscope, image modeling (or simulation) was needed to relate the image to the object. Optical images were simulated by solving Maxwell's equations for the object and optical system used [3]; scanning electron microscope images are usually simulated by modeling electron-material scattering mechanisms in a Monte Carlo framework [4], and AFM images are simulated by deconvolving the tip shape from the raw image [5]. The object and the microscope are represented in these models by parameterized descriptions, reducing the amount of information the model has to process and the corresponding accuracy of the results. In each case, the microscope scale must be calibrated in a separate process [6].

Maxwell's equations can be difficult to solve for a real microscope image; analytic solutions exist for only a few simple cases. Several numerical approaches can be used: the rigorous coupled waveguide analysis method (RCWA) [7] treats the object as one line of an infinite diffraction grating; other methods include the finite element method (FEM) [8], the finite difference time domain (FDTD) [10], and the integral equation method [11]. Each method involves a different set of assumptions and compromises. RCWA, FEM, and FDTD packages are available commercially and are usually optimized for speed of execution. While the resulting accuracy may be adequate for many purposes, the compromises made for speed

are often not well documented, and for the present purpose, the accuracy of the results was paramount. Consequently, an integral equation method was developed at NIST. This method treats only isolated features and finite arrays; RCWA treats only infinite arrays.

3. The Integral Equation Method for Simulating Microscope Images

To find the fields scattered by an object in an optical microscope for an incident plane monochromatic wave of circular frequency ω, we transformed Maxwell's equations into a set of two two-dimensional (2-D) Helmholtz equations for two scalar functions. We then reduced these equations to integral equations for unknown functions defined on the boundaries between homogeneous regions. We used a method designed to minimize the number of such functions, which resulted in savings of memory requirements and execution time. We solved these integral equations by the point-matching method and then computed the field components by integration. A plane wave has a propagation vector whose magnitude, k, is given by $k^2 = \varepsilon\mu\omega^2$ in terms of the permittivity ε and the permeability μ of the medium where it propagates.

We modeled the image created by an optical microscope in the transmission mode of an infinite Cr line of finite width on a quartz substrate of finite thickness and of a space in a Cr layer on the same quartz substrate. To use the same model for lines and spaces, we approximate the two chrome regions by lines of a width that is large compared to the wavelength, with the space in between. Chrome has a large but finite conductivity, and we assumed that the quartz layer was transparent.

As described in this Section and in the Appendix, we chose the z-axis along the line and the y axis perpendicular to the substrate. This coordinate system was originally chosen to describe the scattering of electromagnetic fields by cylindrical objects, where the z axis is parallel to the generator of the cylinders. When the geometry of the problem is invariant under translations in the z-direction, we can show that the electromagnetic fields can be expressed in terms of the longitudinal components of the fields, E_z and H_z, as detailed in Eqs. (A1) to (A7) in [12]. These fields satisfy the 2-D Helmholtz equation,

$$(\nabla_\perp^2 + k_\perp^2)E_z(x,y) = 0, \quad (\nabla_\perp^2 + k_\perp^2)H_z(x,y) = 0, \quad (1)$$

where the perpendicular parts of the gradient operator and of the propagation vector are defined by

$$\nabla_\perp = \hat{e}_x \partial/\partial x + \hat{e}_y \partial/\partial y, \qquad \vec{k}_\perp = \hat{e}_x k_x + \hat{e}_y k_y, \quad (2)$$

where $\hat{e}_x$ and $\hat{e}_y$ are the unit vectors along the x-axis and the y-axis, respectively. The two longitudinal components of the fields, E_z and H_z, are required if the incident wave has arbitrary polarization and direction of propagation.

We approximated the illumination of the microscope by a set of incident plane waves that scatter independently. To apply the general solutions of the Helmholtz equation that satisfy the radiation condition, we decomposed the fields into homogeneous fields and scattered fields, indicated by superscripts h and sc, respectively. Homogeneous fields are plane waves such as the incident, reflected, and refracted fields. Other than the incident field, they are introduced by a substrate and a layer of finite thickness in the absence of a scatterer. The equations that allowed us to determine the amplitudes of the longitudinal components of the homogeneous fields in terms of the incident fields are given by Eqs. (A12) to (A19) in [12].

To determine the scattered fields in all of space, we derived integral equations for functions defined on the interfaces between the homogeneous regions, as described in the Appendix. We reduced these integral equations to linear algebraic equations by the point-matching method. Once these approximate solutions were found, we determined the fields on a plane parallel to the substrate at a height y_0 above the layer by the integrals in Eqs. (A49) to (A54) in [13]. For a wavelength of 365 nm and a height of 5 μm, we found that the evanescent fields and the induction fields were negligible compared to the radiation fields. The contribution to the image from a plane wave was then obtained by representing the collection lens by its aperture and magnification, which were used to modify Fourier components of the scattered fields. This process is described in Subsection 6 of the Appendix in [12].

4. The Objects and the Microscope

Figure 3 shows the idealized cross section of an isolated chrome-on-quartz photomask line. This structure, along with values for the related parameters, constitutes the "object model" in the sense of [13]. "Isolated" here means the nearest chrome edge adjacent to this feature on the photomask is sufficiently remote that moving it farther away would not change its FW measurement by an amount more than some tolerance. For our microscope, this means more than about 10 wavelengths for a tolerance of less than 1 nm, and our photomask standards were designed to meet this criterion. All of the image model examples here are for variants of this 2-D (FW, Cr thickness) object.

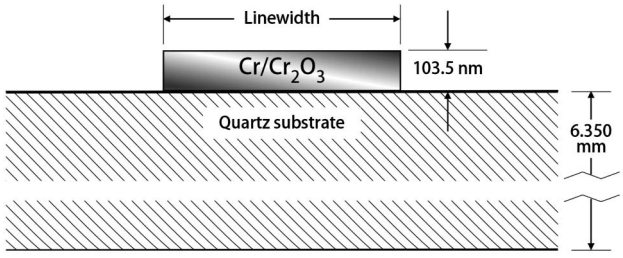

Fig. 3. Cross section of a typical chrome-on-quartz photomask line feature.

The microscope is a full-field optical microscope operating at 365 nm wavelength in the transmission mode with Köhler illumination. Transmission mode is preferred for photomask metrology because the image is simpler than in reflection mode, the contrast is higher, and the substrate baseline intensity (through the clear quartz) is stable and repeatable. The intensity I in the image plane is measured with an on-axis sampling aperture and photomultiplier tube while the object stage is scanned in the x direction, perpendicular to the line being measured (here the z-axis is the microscope optical axis, and the x- and y-axes lie in the object plane or the conjugate image plane). Intensity I and stage position x are sampled synchronously, and the resulting image is an array of intensity I and an array of position x data points, which together form the image curve $I(x)$. The intensity was scaled so that the dark current (illumination shutter closed) is represented by $I = 0$, and the intensity through the clear quartz by $I = 1$. Intensity calibration was not required as long as the intensity detector was linear; the microscope x-scale was calibrated using a pitch standard (SRM 2800 [6]) that had been calibrated separately on the NIST Linescale Interferometer.

5. Focus

In a real microscope, it can be difficult to determine if an object is "in focus," and in fact, if the object is a wavelength or thicker, then there may be no single "best focus." In addition, it is difficult to instrument a microscope to accurately measure the physical distance from the objective lens to the object or substrate, so the focus criterion usually applies to the image itself. The focus criterion adopted here was based on the acutance ∇I in the image, or dI/dx where a chrome line lies along the y-axis and the x-axis is perpendicular to the edge. Images were taken over a range of focal distances z; the image with the highest acutance was the one with the best focus, or the best focus could be found more accurately by polynomial interpolation of $\nabla I(z)$ between images.

In addition, the images were modeled over a range of 21 focal steps spaced 50 nm apart in the z-direction, with the z-axis origin at the substrate surface. The maximum acutance was found for each image, and the best focus was found by interpolation. Since the chrome thickness was only about one-third of the wavelength, there was only one maximum acutance in this range. Results are shown in Fig. 4 for isolated chrome lines and spaces, where the horizontal dashed line is the top of the chrome. It is particularly important to use the same focus criterion for the real microscope and for the image simulations.

An alternative approach uses this stack of through-focus images as "the image" for both real microscope images and simulated images [14]. This obviates the need for a definition of "best focus," but aligning the focus steps between real and simulated images may be difficult.

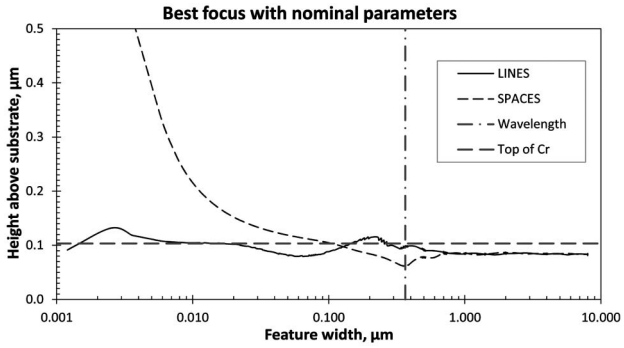

Fig. 4. Image best focus as function of FW for the photomask features in Fig. 5. Best focus is defined here as maximum acutance.

6. Variable Threshold Method

By modeling the microscope images of isolated chrome lines and spaces over a range of FWs, we can calculate the image intensity at the chrome's edge at best focus as a function of FW, shown in Fig. 5 for the 365 nm wavelength. For features significantly larger than the wavelength, the edge threshold intensity is nearly independent of the FW and is the same for both lines and spaces because the right and left edges of a feature are separated sufficiently to nearly remove the optical proximity effects.

Now a feature's edges can be identified in a real image by finding the positions of the appropriate intensity from Fig. 5. This is an iterative process because the edge threshold intensity is a function of FW, and the apparent FW depends on the threshold intensity; this process converges rapidly in practice, however.

Figure 6(b) shows the measurement error using the variable threshold method; the errors shown result from the fact that the edge threshold lies between samples in a digitized image, and linear interpolation was used for this example. Figure 6(a) shows the two-point calibration error from Fig. 2 at the same scale for comparison. Clearly the use of image modeling permits optical measurements of object dimensions well below the wavelength of light used.

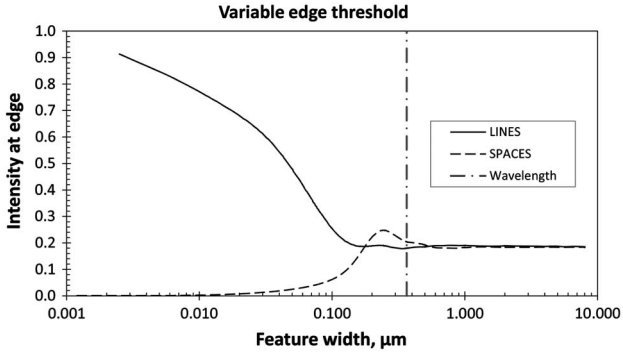

Fig. 5. Image intensity at the edge of an isolated line or space as function of FW. Lines and spaces behave differently for FWs smaller than the wavelength.

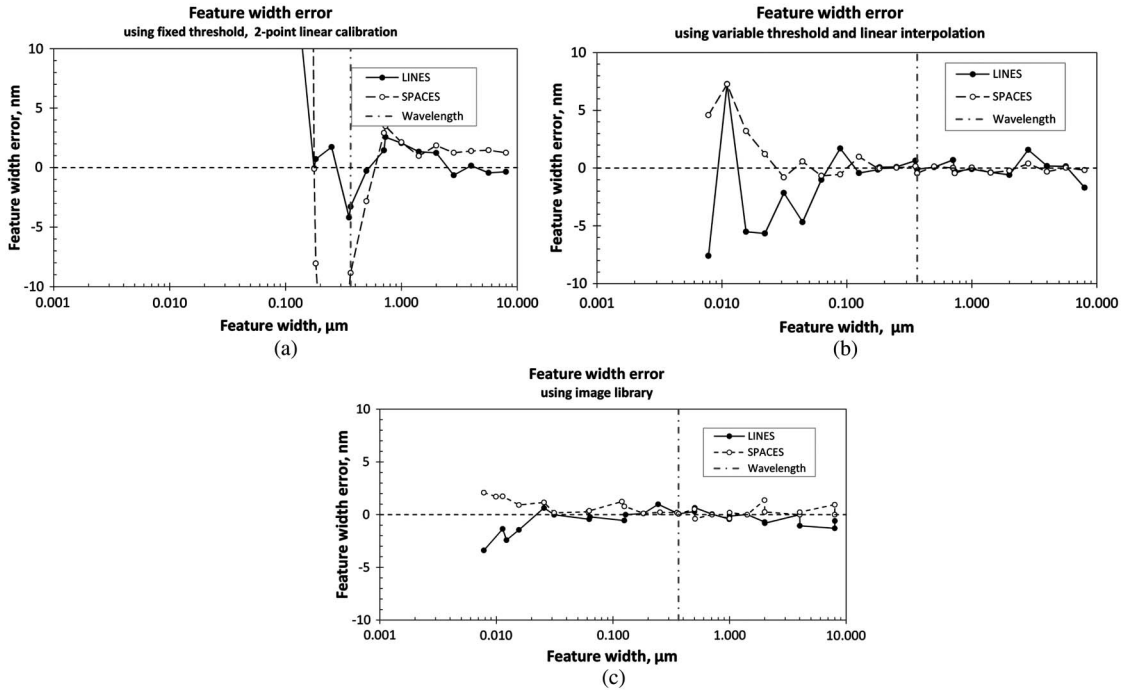

Fig. 6. Calibration FW errors (a) replotted from Fig. 2 for comparison with Figs. 6(b) and 6(c), (b) using the variable threshold method of image edge identification (errors are largely due to interpolation of sampled data), and (c) using the image library method of extracting data from a microscope image. All plotted to the same scale.

7. Parametric Measurement Uncertainty

Every measurement has a purpose, and every measurement has an uncertainty. The purpose of the measurement can help establish a measurement tolerance or the uncertainty confidence interval that can be tolerated. Evaluating the measurement uncertainty will establish whether it is in tolerance or not; i.e., sufficiently accurate to meet the purpose of the measurement [2].

The image model used must accurately reflect the microscope imaging process. Several parameters that describe the instrument and the object can affect the microscope image, and their values are inputs to the modeling program. These values are subject to measurement uncertainty, and these uncertainties propagate through the model, resulting in uncertainty in the simulated image and in the inferred FW. The best estimate of the value for each parameter was used in the model. The error in this estimate, by its nature, was not known; only the error probability distribution or the uncertainty of the estimate was known [15].

NIST's length calibration measurements are traceable to the definition of the meter, so the errors from all significant sources were estimated. The parameters included in this study are listed in Table 1.

In Table 1, NA refers to numerical aperture, and n and k are the real and imaginary parts of the index of refraction.

If $\{P_i\}$ is the set of all parameters affecting the image and the error in the ith parameter is δP_i, the corresponding FW error component $\delta \mathrm{FW}_i$ is [15]

$$\delta \mathrm{FW}_i = \partial \mathrm{FW}/\partial P_i \delta P_i \tag{3}$$

for small parameter errors. The corresponding standard parametric uncertainty component of FW is

$$u_{pi}(\mathrm{FW}) = u(P_i)|\partial \mathrm{FW}/\partial P_i|, \tag{4}$$

where $u(P_i)$ is the standard uncertainty of the value of parameter P_i. The combined standard parametric uncertainty of FW is

$$u_{\mathrm{param}}(\mathrm{FW}) = \sqrt{\sum_i [u(P_i)\partial \mathrm{FW}/\partial P_i]^2}, \tag{5}$$

summed over all of the relevant parameters P_i.

The combined standard uncertainty for FW measurements $u(\mathrm{FW})$ can be stated as

$$u(\mathrm{FW}) = \sqrt{[\sigma^2 + u_{\mathrm{param}}^2 + u_{\mathrm{other}}^2]}, \tag{6}$$

where σ is the measurement repeatability and u_{other} includes the microscope scale calibration, model calculation inaccuracies, differences between the real object and its parametric description, and other systematic effects. Room temperature and humidity fluctuations, vibration, etc., were included in the repeatability because each feature was measured multiple times at time intervals long enough to randomize these environmental fluctuations.

This concept can be generalized. Any parameter could be the measurand, and the FW could be treated as another parameter. The optical imaging model

relates the parameters to the image intensity $I(x,y)$ and can be expressed as $I = F(\{P_i\})$. Any one of these parameters, P_k, may be the apparent value of a measurand, and its parametric uncertainty depends on the others. Specifically,

$$u_{\text{param}}(P_k) = \sqrt{\sum_i (\partial P_k/\partial P_i)^2 u^2(P_i)}, \qquad i \neq k. \quad (7)$$

In most cases, the quantities $\partial P_k/\partial P_i$ can be determined only through image modeling.

The $u(P_i)$ were determined from independent measurements of the P_i or from other data such as manufacturing tolerances, and the $\partial \text{FW}/\partial P_i$ was determined by modeling the microscope image with perturbations of P_i and calculating the slope $\Delta \text{FW}/\Delta P_i$ at the nominal value of P_i and over a representative range of FWs for both lines and spaces. Second-order effects and correlations among the parameters $\partial^2 \text{FW}/\partial P_i \partial P_j$ were not included because of the magnitude of computation time required, but the treatment was straightforward [15–19].

Results of these calculations of $u_{\text{param}}(\text{FW})$ for the variable threshold method of image interpretation and using the values in Table 1 are shown in Fig. 6(b) [20]. Standard uncertainties were less than 10 nm for FWs greater than the wavelength, but then rose to grandiose levels for smaller features. The reason is that parameter errors gave rise to edge threshold errors δThresh; then $\delta\text{FW} = 2\,\delta\text{Thresh}/(dI/dx)$ and dI/dx diminished at smaller feature sizes (Fig. 7). The factor 2 arose from the fact that the edges are displaced in opposite directions when the threshold was displaced.

Feature sizes on production photomasks can be smaller than 100 nm. While the variable threshold method is capable of producing accurate FW measurements [Fig. 6(b)], for small but important feature sizes, it cannot gracefully tolerate the parameter uncertainties typically encountered, leading to unacceptable measurement uncertainties (Fig. 8).

8. Image Library Method

A 2-D image $I(x,y)$ or a three-dimensional through-focus image $I(x,y,z)$, even if not digitized, contains a finite amount of information about the object by virtue of the finite spatial frequency passband of the microscope. According to §0.1 of [21], this is insufficient information to entirely reconstruct the object. The image may contain sufficient information to synthesize a parametric description of the object if the parameter space can be made sufficiently small by reducing the number of parameters, by assigning tolerances to the parameters, and by adding prior knowledge about the object.

A tractable way of implementing this feedback loop is to create, prior to the measurement, a multidimensional library of simulated images covering the relevant range of parameter space, where FW can be considered one of the parameters [22]. The object then has the parameter values of the simulated image that most closely matches its real image (or interpolated, if necessary). Prior knowledge about the values and probability distributions of some of the parameters can be used to narrow the search volume and reduce the probability of nonunique matches. This method moves the time-consuming computations offline; the library can be reused for new measurements as appropriate and will grow as more objects are simulated.

To use this approach, an image difference metric is required, and the one chosen for this purpose was

$$Q_{jk} = \sqrt{\frac{1}{n}\sum_{i=1}^{n} [I_j(x_i) - I_k(x_i)]^2}, \quad (8)$$

where $I_j(x)$ and $I_k(x)$ are two photomask line feature images to be compared and n is the number of image samples compared. These are digitized (sampled) images; usually one will be a real microscope image and the other a simulated image. They must be aligned in the x-axis and have the same sampling interval Δx; some resampling may be required to accomplish this. In addition, the image intensities must be normalized in the same way, e.g., $I = 1$ through the clear quartz substrate for both. When $I_j(x) = I_k(x)$ the two images are identical and $Q_{jk} = 0$. Other metrics could be used, but Q_{jk} is probably the simplest.

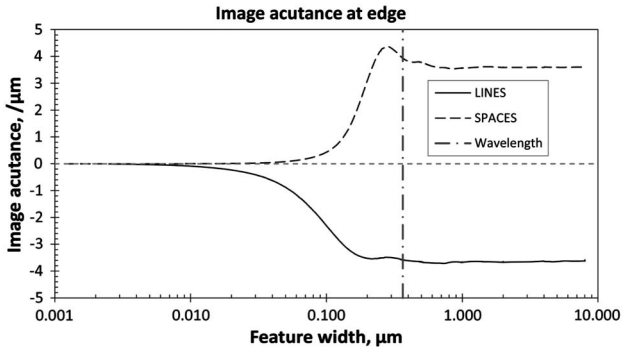

Fig. 7. Image acutance at feature edge of isolated lines and spaces.

Table 1. Imaging Parameters Used Here and Their Uncertainties

	Parameter	Nominal Value	Standard Uncertainty
Microscope parameters	Wavelength	365 nm	3 nm
	Illumination NA	0.6	0.1
	Objective NA	0.9	0.05
	Defocus	0	100 nm
	Sampling aperture (pixel size) in the object plane	100 nm	50 nm
Object parameters	Cr thickness	103.5 nm	3 nm
	Cr n	1.843	0.5
	Cr k	2.195	0.5
	Quartz n	1.475	0
	Quartz k	0	0

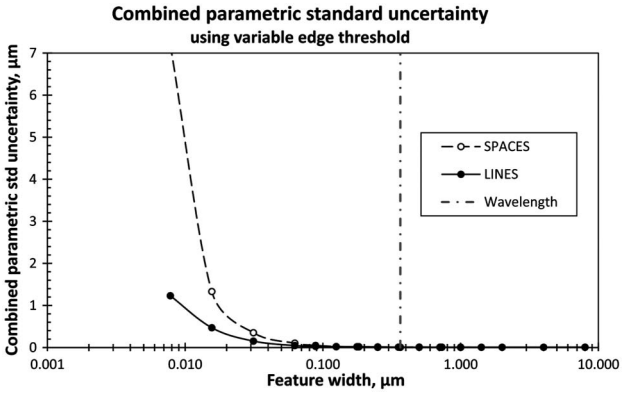

Fig. 8. Combined parametric standard uncertainty using the variable edge threshold method and the parameter values and their uncertainties listed in Table 1.

For this study, a one-dimensional (1-D) image library was constructed for 19 lines and 19 spaces with the nominal parameters in Table 1 and FWs of (0.0078, 0.0156, 0.0313, 0.0625, 0.0884, 0.1250, 0.1768, 0.1825, 0.2500, 0.3536, 0.3650, 0.5000, 0.7071, 0.7300, 1.0000, 1.4142, 2.0000, 4.0000, and 8.0000 μm). In order to determine $\partial \mathrm{FW}/\partial P_i$, each of these was surrounded with 16 satellite images at 2.6 nm FW intervals. This 1-D library has a total of 632 simulated images with nominal parameters, each with 21 focus levels, with $x = 0$ at the feature center and $\Delta x = 6$ nm.

Ignoring for the moment the effect of parameter uncertainties, Fig. 6(c) shows FW errors using this library of images. These errors can be reduced by using a more sophisticated method of finding the minimum Q_{jk} (or simply Q). Figure 9 shows the Qs found when matching each nominal FW to its satellites.

9. Parametric Uncertainty with the Image Library Method

In order to determine $\partial \mathrm{FW}/\partial P$ images were calculated with parameter values differing from their nominal values one parameter at a time and each at best focus (because the microscope is always focused by the same criterion). The resulting images were compared to the library of images (all with nominal parameters) over a range of nearby FWs, and the Qs were calculated. The putative parameter error was δP, and the corresponding apparent FW error δFW was found by finding the library image having the best match (that for which Q was minimum). This process was refined by fitting $Q(\delta \mathrm{FW})$ to a polynomial to interpolate Q between library images and finding that the δFW that minimizes Q. $\partial \mathrm{FW}/\partial P$ is the slope of the polynomial fit for $\delta \mathrm{FW}(\delta P)$ evaluated at $\delta P = 0$.

Figure 10 shows Qs for variations in illumination NA for 125 nm lines and spaces. The image of a 125 nm line with parameter error δP looks like the image of a $(125 + \delta \mathrm{FW})$ nm line with no parameter error. This process was repeated for a range of values of each parameter in Table 1 (except wavelength). The Qs were calculated over an x range of FW + 5λ (0.9125 μm outside of each feature edge).

Then each parametric uncertainty component of the FW was calculated from $u_{\mathrm{param},i}(\mathrm{FW}) = u(P_i)|\partial \mathrm{FW}/\partial P_i|$ and the combined parametric uncertainty from $u_{\mathrm{param}}(\mathrm{FW}) = \sqrt{\sum [u(P_i)\partial \mathrm{FW}/\partial P_i]^2}$. This result is shown in Fig. 11(a), and the corresponding edge threshold result is replotted to the same scale in Fig. 11(b) for comparison. Parametric uncertainty for the image library method is slightly greater than for the edge threshold method for FWs greater than the wavelength, peaks still higher around the wavelength, but then diminishes for smaller features in dramatic contrast to the threshold method. For features larger than the wavelength, the image width scales directly with the FW, and the edge threshold method measures only that part of the image most directly related to its width.

The parametric uncertainty peaks at the wavelength are attributed to the fact that the nature of the images changes at FWs near the wavelength. For larger features, the width of the image is

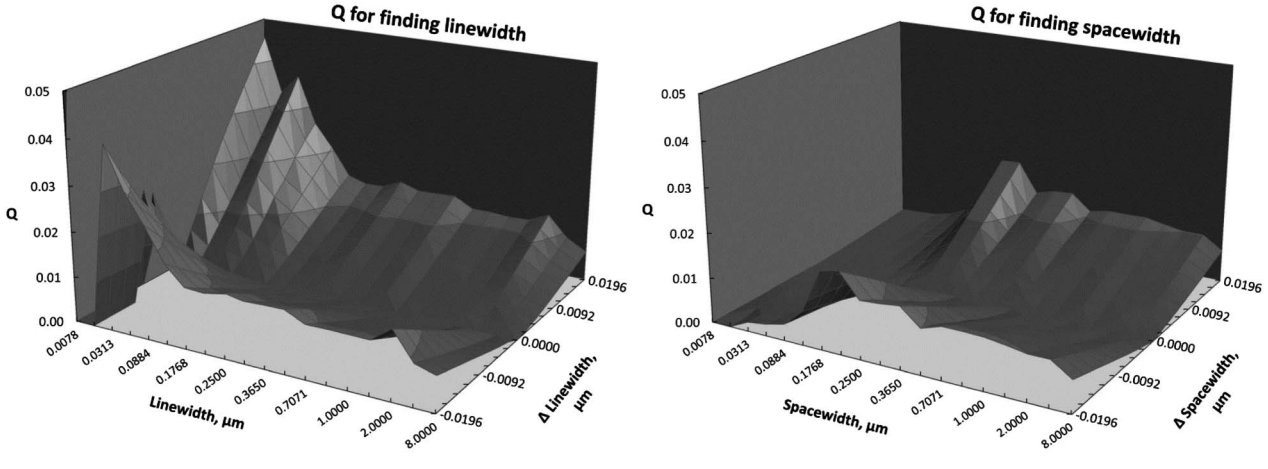

(a) (b)

Fig. 9. Shape of image-matching metric Q surface for identifying the FW in an image; minimum Q points to the best library image match. (a) Isolated lines, (b) isolated spaces. Q is small at small spacewidths because the image intensity is small; see Fig. 11(b).

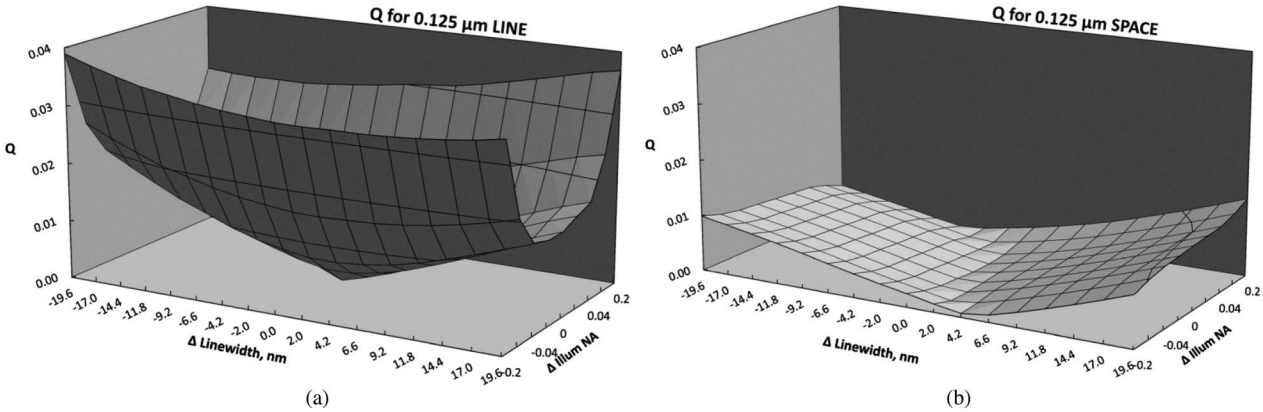

Fig. 10. Shape of image-matching metric Q surface for finding the apparent FW in an image when the illumination NA is in error by δNA; minimum Q points to the best library image match. (a) 125 nm line and (b) 125 nm space.

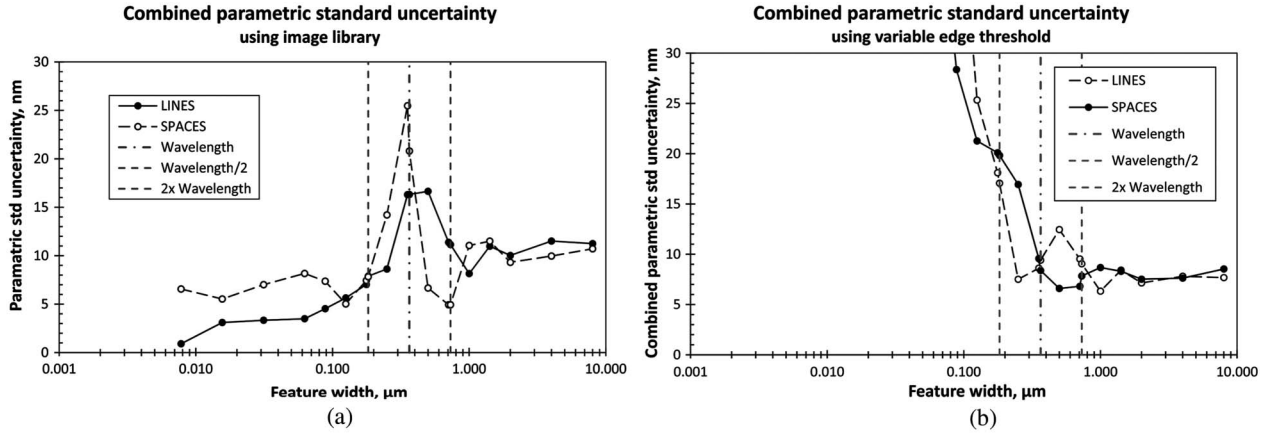

Fig. 11. Combined parametric standard uncertainty for linewidths and spacewidths using the parameter values and uncertainties in Table 1 and (a) the library-matching method of finding the best match feature width; (b) the variable edge threshold method of extracting feature width data (the same data as Fig. 8, rescaled for comparison).

proportional to the width of the feature, and the contrast $(I_{\max} - I_{\min})/(I_{\max} + I_{\min}) \approx 1$; for smaller features, the width of the image does not change much, but the contrast is a monotonic function of FW (Fig. 12). The transition region between these is where the parametric uncertainty is largest. The good news is that this uncertainty component is tolerable for smaller FW and even appears to decline.

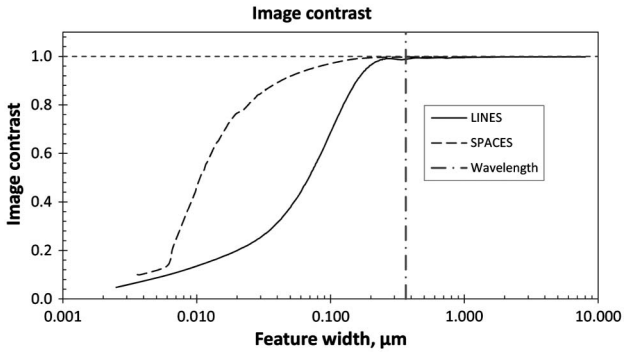

Fig. 12. Image contrast for photomask lines and spaces. The contrast is nearly independent of feature width for features larger than the wavelength but varies monotonically for smaller features.

Contrary to dense arrays, there appears to be no theoretical lower limit to the isolated feature size that can be measured optically (signal-to-noise ratio may be a practical limiting factor). For comparison, the measurement repeatability σ in our laboratory (pooled standard deviation of the mean of over 4,000 linewidth and spacewidth measurements ranging from 150 nm to 32 μm) was less than 3 nm.

The overall uncertainty can be reduced by reducing the parameter uncertainties in Table 1 (e.g., by better measurements of the parameters). The leading contributors to the parametric uncertainty can be identified from the $u(P_i)|\partial \mathrm{FW}/\partial P_i|$ at the FWs of interest (Fig. 13).

10. Model Accuracy

No imaging model is perfect; errors can arise from the discretization of Maxwell's equations for digital computation, programming assumptions, programming errors, etc. In principle, the accuracy of the model at a point in parameter space can be assessed by acquiring the image of a real object with the same object parameters with a real microscope with the same microscope parameters, then comparing that image with the modeled image. This would require

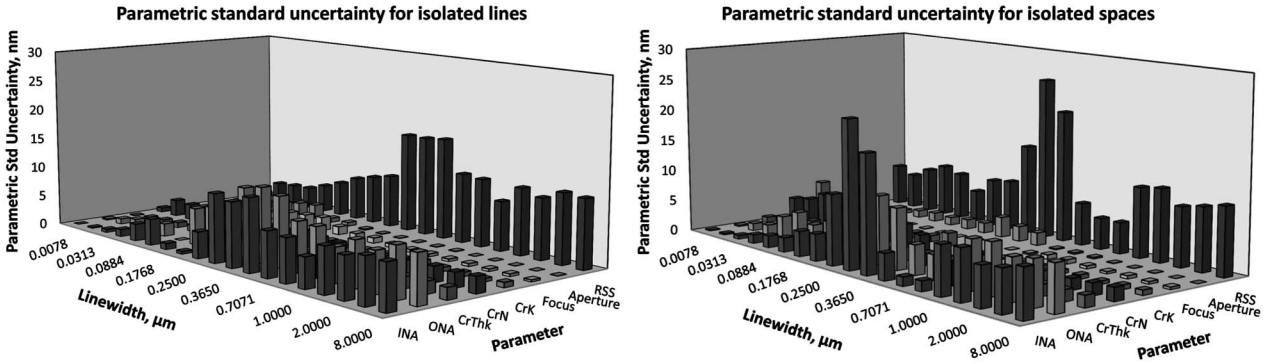

Fig. 13. Separate parametric uncertainty components contributing to the combined parametric feature width uncertainty in Fig. 11(a). (a) Isolated lines; the major components appear to be microscope illumination and objective NA. (b) Isolated spaces; the major component appears to be microscope illumination NA.

that the object and microscope be completely described by finite sets of parameters whose values are accurately known. Even if a real object and a real microscope could be adequately described by a finite number, N, of parameters, the values of those parameters would occupy an N-dimensional region whose cross sections are Gaussian probability distributions, not discrete points [23]. Alternatively, perhaps one could find an ideal object for which an analytic solution exists and compare that with the model result.

Both methods require objects that do not exist. Perhaps the best that can be done is to compare different models with each other when modeling the same ideal object and ideal microscope. Differences in the results should be compared on a meaningful basis, such as apparent parameter differences, to assess their significance, and should then be used to help track down the sources of discrepancies and perhaps place a lower limit on model uncertainty.

Because of their complexity, the imaging models described above are evaluated numerically, necessitating decisions about calculation intervals Δx (and Δt for the FDTD method), grid resolution for the FEM methods, number of incident illumination angles, number of terms to carry in an infinite series, etc. These computation parameters can be used to establish the tradeoff between execution speed and accuracy, but their effects on model accuracy must be evaluated by modeling the same object with different values of computation parameters [24]. Then these parameters can be chosen so that the resulting computation errors are less than a tolerance, which can be included in the measurement uncertainty.

11. Real Photomasks, True Value, Definitional Uncertainty

Real binary (containing only nominally opaque and clear areas) chrome photomasks are fabricated by depositing a proprietary gradient index inhomogeneous thin film of Cr, Cr_2O_3, and other compounds on a fused quartz substrate and then etching this film to form the desired features. As a consequence of this composition, the etching rate is not constant with Cr depth, and feature sidewalls are not straight and vertical like those in Fig. 3, as confirmed by AFM measurements. The question arises, "What is the true value of the linewidth of such a feature?" The term "true value" is defined in [21, §2.11] as "a quantity value consistent with the definition of a quantity," along with a discussion of definitional uncertainty. That discussion is beyond the scope of this paper but must be considered when making measurements of the kind described here. Further discussion regarding photomasks and definitional uncertainty can be found in [2].

The chrome n and k values cited in Table 1 are equivalent values for homogeneous chrome derived from spectroscopic ellipsometry measurements on NIST photomasks. The parametric error resulting from the assumption of homogeneous chrome was assessed by modeling the gradient index case and comparing the results with the homogeneous case. Computation time was significantly longer, but the modeled image differences were small.

12. Conclusion

Modeling of the image-forming process is a key ingredient in the dimensional measurements of small objects in a microscope. The approach described here can be applied to optical microscopes — yielding accurate measurements well below the illumination wavelength — scanning electron microscopes [22], and perhaps to scanning probe microscopes. Despite their limited image resolution, optical microscopes can measure nanoscale objects and have practical advantages of speed, noncontact imaging, and cost over SEMs and AFM.

The same procedures can be used for transmission and reflection mode optical images, other objects such as nanospheres, contact holes on photomasks, etc., by using the appropriate model; the numerical results will, of course, be different. Uncertainties may be improved by more accurate measurements of the parameters, using a shorter wavelength, using confocal imaging, etc.

A final caveat, second-order effects and their possible covariance, is not included here. Treatment of higher order effects is described in [16].

Appendix A

For the configurations shown in Fig. 14, we defined eight auxiliary fields, U_1, U_2, U_3, U_7, U_1', U_2', U_3', and U_7'. The fields U_1 and U_1' equal E_z^{sc} and H_z^{sc} in V_1; satisfy the same Helmholtz equation in V_2, V_3, and V_7 as in V_1; are continuous everywhere; have discontinuous normal derivatives with jumps η_{11} and η_{11}' across C_1, jumps η_{12} and η_{12}' across C_2, and zero jumps across C_3; and satisfy the radiation condition as $y \to -\infty$. They also satisfy the radiation condition as $y \to +\infty$ because in that region they are equal to scattered fields. The fields U_2 and U_2' equal E_z^{sc} and H_z^{sc} in V_2; satisfy the same Helmholtz equation in V_1, V_3, and V_7 as in V_1; are continuous everywhere; have a discontinuous normal derivative with jumps η_{21} and η_{21}' across C_1, jumps η_{23} and η_{23}' across C_3, and a zero jump across C_2; and satisfy the radiation condition as $y \to +\infty$. The fields U_3 and U_3' equal the longitudinal components of the total fields, E_z and H_z, in V_3 and vanish in V_1, V_2, and V_7. The fields U_7 and U_7' equal E_z^{sc} and H_z^{sc} in V_7; satisfy the same Helmholtz equation in V_1, V_2, and V_3 as in V_7; are continuous everywhere; have discontinuous normal derivatives with jumps η_{71} and η_{71}' across C_1, jumps η_{73} and η_{73}' across C_3, jumps η_{70} and η_{70}' across C_0, and a zero jump across C_2; and satisfy the radiation condition as $y \to +\infty$ and as $y \to -\infty$ by definition. These auxiliary fields are given by

$$U_1(\vec{\xi}) = G_{11}\{\eta_{11}\}(\vec{\xi}) + G_{12}\{\eta_{12}\}(\vec{\xi}), \tag{A1}$$

$$U_2(\vec{\xi}) = G_{21}\{\eta_{21}\}(\vec{\xi}) + G_{23}\{\eta_{23}\}(\vec{\xi}), \tag{A2}$$

$$\begin{aligned} U_3(\vec{\xi}) = {} & G_{32}\{\Delta_2(\partial U_3/\partial n)\}(\vec{\xi}) + N_{32}\{\Delta_2 U_3\}(\vec{\xi}) \\ & + G_{33}\{\Delta_3(\partial U_3/\partial n)\}(\vec{\xi}) + N_{33}\{\Delta_3 U_3\}(\vec{\xi}), \end{aligned} \tag{A3}$$

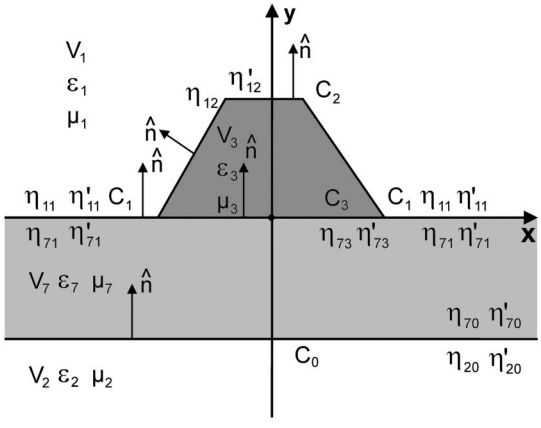

Fig. 14. Scattering by a Cr strip on a quartz layer on a substrate, incidence from below the layer. Unknown boundary functions η_{ij} and η_{ij}' are jumps in the normal derivatives of the fields in V_i across the boundary C_j.

$$U_7(\vec{\xi}) = G_{71}\{\eta_{71}\}(\vec{\xi}) + G_{73}\{\eta_{73}\}(\vec{\xi}) + G_{70}\{\eta_{70}\}(\vec{\xi}),$$

in terms of the functionals $G\{\eta\}$ and $N\{\varphi\}$ defined by

$$G\{\eta\}(\vec{\xi}) = -\frac{i}{4}\int_C ds'\eta(s')H_0^{(1)}(k_\perp R), \tag{A4}$$

$$N\{\phi\}(\vec{\xi}) = \frac{i}{4}\int_C ds'\phi(s')H_1^{(1)}(k_\perp R)k_\perp \hat{n}' \cdot \hat{R}, \tag{A5}$$

where the $H_n^{(1)}$ are Hankel functions, $\vec{\xi}' = \vec{X}(s')$, $\vec{R} = \vec{\xi} - \vec{\xi}'$, $R = |\vec{R}|$, $\hat{R} = \vec{R}/R$, and $\hat{n}' = \hat{n}(s')$, with similar expressions for the other four auxiliary fields. Related functionals are the normal and tangential derivatives of G, N', and N''.

From the continuity conditions, we can express U_3 and U_3' in terms of the homogeneous fields and the unknown boundary functions. We then use the continuity conditions on the tangential components of the fields and the definitions of the auxiliary fields to derive 12 integral equations for the 12 unknown boundary functions, η_{11}, η_{12}, η_{20}, η_{71}, η_{73}, η_{70}, η_{11}', η_{12}', η_{20}', η_{71}', η_{73}', and η_{70}'; for instance,

$$\begin{aligned} & G_{11}^1\{\eta_{11}\} + G_{12}^1\{\eta_{12}\} - G_{71}^1\{\eta_{71}\} - G_{73}^1\{\eta_{73}\} \\ & \quad - G_{70}^1\{\eta_{70}\} = 0, \end{aligned} \tag{A6}$$

$$\begin{aligned} & \frac{1}{2}\eta_{11} + N_{12}'^1\{\eta_{12}\} + \frac{1}{2}\overline{b}_1\eta_{71} - \overline{b}_1 N_{70}'^1\{\eta_{70}\} \\ & \quad - \overline{\beta}_1 N_{11}''^1\{\eta_{11}'\} - \overline{\beta}_1 N_{12}''^1\{\eta_{12}'\} = 0, \end{aligned} \tag{A7}$$

$$\begin{aligned} & [(1/2 + N_{32}^2)G_{11}^2 + b_2 G_{32}^2 N_{11}'^2]\{\eta_{11}\} \\ & + [(1/2 + N_{32}^2)G_{12}^2 + b_2 G_{32}^2(1/2 + N_{12}'^2)]\{\eta_{12}\} \\ & - N_{33}^2 G_{71}^3\{\eta_{71}\} + (1/2\overline{b}_3 G_{33}^2 - N_{33}^2 G_{73}^3)\{\eta_{73}\} \\ & - (\overline{b}_3 G_{33}^2 N_{70}'^3 + N_{33}^2 G_{70}^3)\{\eta_{70}\} + \beta_2 G_{32}^2 N_{11}''^2\{\eta_{11}'\} \\ & + \beta_2 G_{32}^2 N_{12}''^2\{\eta_{12}'\} - \overline{\beta}_3 G_{33}^2 N_{71}''^3\{\eta_{71}'\} - \overline{\beta}_3 G_{33}^2 N_{73}''^3\{\eta_{73}'\} \\ & - \overline{\beta}_3 G_{33}^2 N_{70}''^3\{\eta_{70}'\} \\ & = -(1/2 + N_{32}^2)\{E_z^{h1}\} - b_2 G_{32}^2\{\partial E_z^{h1}/\partial n\} + N_{33}^2\{E_z^{h7}\} \\ & \quad + \overline{b}_3 G_{33}^2\{\partial E_z^{h7}/\partial n\} - \beta_2 G_{32}^2\{\partial H_z^{h1}/\partial s\} \\ & \quad + \overline{\beta}_3 G_{33}^2\{\partial H_z^{h7}/\partial s\}, \end{aligned} \tag{A8}$$

where coefficients such as b_2 and β_2 are functions of the constants of the wave and of the media. The functionals $N_{11}'^1$, $N_{71}'^1$, $N_{20}'^0$, $N_{70}'^0$, $N_{71}'^3$, $N_{73}'^3$, $N_{73}'^1$, and N_{33}^3 vanish, and they have been eliminated from the equations. We can solve for η_{71}, η_{20}, η_{71}', and η_{20}' from four of the integral equations and substitute them into the other eight equations that can then be solved for the eight remaining variables.

References and Notes

1. NIST SRM 2059 Photomask Linewidth Standard is available from the Office of Standard Reference Materials, NIST, EM 205, Gaithersburg, MD 20899. See sample certificate at https://www-s.nist.gov/srmors/certificates/view_certGIF.cfm?certificate=2059.
2. J. Potzick, "Metrology and process control: dealing with measurement uncertainty," Proc. SPIE **7638**, 76381U (2010).
3. D. Nyyssonen, "Linewidth measurement with an optical microscope: the effect of operating conditions on the image profile," Appl. Opt. **16**, 2223–2230 (1977).
4. J. Villarrubia, A. Vladar, and M. Postek, "Scanning electron microscope dimensional metrology using a model-based library," Surf. Interface Anal. **37**, 951–958, doi:10.1002/sia.2087 (2005).
5. J. Villarrubia, "Morphological estimation of tip geometry for scanned probe microscopy," Surf. Sci. **321**, 287–300 (1994).
6. NIST SRM 2800 Microscope Pitch Standard is available from the Office of Standard Reference Materials, NIST, EM 205, Gaithersburg, MD 20899. For details see sample certificate at https://www-s.nist.gov/srmors/certificates/view_certGIF.cfm?certificate=2800.
7. M. Davidson, "A modal model for diffraction gratings," J. Mod. Opt. **50**, 1817–1834 (2003).
8. R. F. Harrington, *Time-Harmonic Electromagnetic Fields* (McGraw-Hill, 1961).
9. R. F. Harrington, *Field Computations by Moment Methods* (Krieger, 1982).
10. A. Taflove and S. C. Hagness, *Computational Electrodynamics, the Finite-Difference Time-Domain Method*, 3rd ed. (Artech House, 2005).
11. E. Marx and J. Potzick, "Simulation of optical microscope images for photomask feature size measurements," in *Proceedings of 2005 IEEE Antennas and Propagation Society International Symposium* (IEEE, 2005), pp. 2116–2119.
12. E. Marx, "Images of strips on and trenches in substrates," Appl. Opt. **46**, 5571–5587 (2007).
13. SEMI Standard P35, "Terminology for microlithography metrology," SEMI International Standards, San Jose, California.
14. R. Attota, R. M. Silver, and J. Potzick, "Optical illumination and critical dimension analysis using the through-focus focus metric," Proc. SPIE **6289**, 62890Q (2006).
15. Joint Committee for Guides in Metrology, *JCGM 100:2008, Evaluation of Measurement Data — Guide to the Expression of Uncertainty in Measurement* (JCGM, 2008), http://www.bipm.org/en/publications/guides/gum.html.
16. B. Taylor and C. Kuyatt, "Guidelines for evaluating and expressing the uncertainty of NIST measurement results," NIST Technical Note 1297 (National Institute of Standards and Technology, 1994).
17. R. Silver, T. Germer, R. Attota, B. Barnes, B. Bunday, J. Allgair, E. Marx, and J. Jun, "Fundamental limits optical critical dimension metrology: a simulation study," Proc. SPIE **6518**, 65180U (2007).
18. R. M. Silver, N. F. Zhang, B. Barnes, H. Zhou, A. Heckert, R. Dixson, T. Germer, and B. Bunday, "Improving optical measurement accuracy using multi-technique nested uncertainties," Proc. SPIE **7272**, 727202 (2009).
19. R. M. Silver, N. F. Zhang, B. M. Barnes, H. Zhou, J. Qin, and R. Dixson, "Nested uncertainties and hybrid metrology to improve measurement accuracy," Proc. SPIE **7971**, 797116 (2011).
20. J. Potzick, E. Marx, and M. Davidson, "Parametric uncertainty in optical image modeling," Proc. SPIE **6349**, 63494U (2006).
21. International Organization for Standardization, *ISO/IEC Guide 99:2007, International Vocabulary of Metrology — Basic and General Concepts and Associated Terms (VIM)*, 3rd ed. (ISO, 2007), http://www.bipm.org/en/publications/guides/vim.html.
22. C. Frase, D. Gnieser, and H. Bosse, "Model-based SEM for dimensional metrology tasks in semiconductor and mask industry," J. Phys. D **42**, 183001 (2009).
23. J. Potzick, "Accuracy and traceability in dimensional measurements," Proc. SPIE **3332**, 471–479 (1998).
24. E. Marx and J. Potzick, "Computational parameters in simulation of microscope images," PIERS Online **5**, 11–15 (2009).